PNAS
www.pnas.org

Supplementary Information for

ALS-linked PFN1 variants exhibit loss- and gain-of-functions in the context of formin-induced actin polymerization

Eric J. Schmidt[1,5], Salome Funes[1,5], Jeanne E. McKeon[1,7], Brittany R. Morgan[2], Sivakumar Boopathy[1,7], Lauren C. O'Connor[3], Osman Bilsel[2,7], Francesca Massi[2], Antoine Jégou[4], Daryl A. Bosco[1,2,6,*]

*To whom correspondence should be addressed: Daryl A. Bosco: Department of Neurology, University of Massachusetts Medical Center, Worcester, MA 01605; Daryl.Bosco@umassmed.edu; Tel. (774) 455-3745; Fax. (508) 856-6750

This PDF file includes:

Other supplementary materials for this manuscript include the following:

Supplementary text: Materials and Methods (**continued from main text**)

SDS-gel electrophoresis and Western blot analysis

Total protein was measured with a Bicinchoninic Acid (BCA) kit (Thermo #23227). Laemmli gel-loading buffer was added to cell lysates and incubated at 95°C for 5 minutes. The ladder (Bio-Rad Precision Plus; 1610374) and lysate samples were electrophoresed through a 15% or 4-20% (Bio-Rad, 456-1094) polyacrylamide gel at 200V and then transferred for 1h at 100V. Western blots were processed using the Li-Cor Odyssey system (ODY-2215) and densitometry measurements were performed using ImageStudio Lite (Li-Cor, v5.2.5).

Immunofluorescence analysis

Cells plated on coverslips were fixed with 4% paraformaldehyde (Fisher Scientific, AAA1131336) at ambient temperature for 15 minutes, permeabilized with 1% Triton X-100 (Sigma, T9284) for 10 min and probed with the different antibodies described below for 1h. The coverslips were washed and incubated with secondary antibodies as described before (1). Cells were counterstained with DAPI (Sigma-Aldrich, D9542) and coverslips were mounted with ProLong Gold anti-fade reagent (Invitrogen, P36930). Images were acquired with a Leica DMI 6000B inverted fluorescent microscope with a 40X air objective or a 63X oil-immersion objective and Leica DFC365 FX camera using AF6000 Leica Software v3.1.0 (Leica Microsystems). Stacked images (z=0.2µm) were collected and presented as deconvolved maximum projections. Within each experiment, acquisition settings were identical for all the sample conditions. Brightness and contrast were equally adjusted post-acquisition across all images to facilitate protein visualization.

Antibodies used in this study.

Target	Species	Antibody	Dilution (WB)	Dilution (IF)
Diaph1	Rabbit	Proteintech; 20624-1-AP	1:500	1:100
Diaph2	Mouse	Santa Cruz; sc-55539	1:200	
FMNL1	Mouse	Santa Cruz; sc-390023	1:120	
FMNL1	Rabbit	Proteintech; 10395-1-AP		1:100
V5	Mouse	Invitrogen; R960-25	1:2000	1:1000
Pfn1	Rabbit	Sigma; P7749	1:1000	
GAPDH	Rabbit	Sigma; G9545	1:10000	
NCKAP1	Rabbit	Novus; NBP2-19491	1:500	

Immunoprecipitation of V5-PFN1

All steps from cell lysis to gel excision were performed in a BSL 2-plus tissue culture hood to prevent keratin contamination. Cells were plated at 10^6 cells/plate in 10cm plates and concurrently induced with 1 µg/ml doxycycline. After 48 hours, the media was discarded and plates were washed with 10 mL PBS. Cells were lysed and scraped with 960 µl lysis buffer (25 mM HEPES (Sigma H3375), 25 mM KCl (Sigma P9541), 5 mM EDTA (Fisher; E478-500), 1% NP-40 (MP Biomedicals; 198596), and 10% v/v glycerol ((Acros; 15982–0010) in water; pH 7.0) supplemented with protease inhibitors (Roche 11836170001) and centrifuged for 10 min at 13K RPM at 4°C. The supernatant was saved and assessed for total protein content using a Bicinchoninic Acid (BCA) kit (Thermo #23227). Because V5-PFN1 C71G is destabilized and expressed at lower levels than other PFN1 variants (2), the PFN1 WT, M114T, and G118V samples were diluted with V5 lysate and lysis buffer such that all samples had the same levels of V5-PFN1 and total protein. For each sample, 100 µl V5 paramagnetic bead slurry (Medical and Biological Laboratories Co, M167-11) was washed three times with 100 µl lysis buffer, and 320 µg lysate (in 400 µl) was added

to the beads and incubated with end-over-end rotation for 1 hr at ambient temperature. An equal volume of each lysate was reserved as an IP input sample. Beads were collected with a magnetic rack and the supernatant removed. Beads were washed 3 times for 5 min with rotation in 400 µl lysis buffer. V5-PFN1 proteins were eluted with 20 µl glycine (1M, pH 2-2.5, Santa Cruz sc-295018) at 70° for 10 min while shaking at 400 rotations per minute (rpm) and manually mixing every 2.5 minutes. The eluate was collected for SDS-gel electrophoresis prior to mass spectrometry analysis. Three independent IPs for MS were performed. An additional three independent biological replicates were performed for the Western blot validation analysis. For each biological replicate, all five V5 lines were included and processed in parallel as described herein.

Sample preparation for mass spectrometry

IP eluates for mass spectrometry (MS) analyses were run approximately 1 cm into a 4-20% gradient gel (Bio-Rad 456-1094) and stained with coomassie brilliant blue (Denville E2700). The band from each lane was excised, cut into 1x1 mm cubes and placed into 1.5 mL eppendorf tubes with 1mL of water for 30 min. The water was removed and 200µl of 250 mM ammonium bicarbonate (Acros Organics, Thermo Fisher Scientific, 393212500) was added, followed by 20 µl of a 45 mM solution of 1,4 dithiothreitol (DTT; Calbiochem, Millipore Sigma, 233153). Samples were incubated at 50°C for 30 min, and then allowed to cool to ambient temperature before adding 20 µl of a 100 mM iodoacetamide (Sigma-Aldrich, I-6125) for 30 min. The gel slices were then washed twice with 1 mL water before adding 1mL of 50:50 (50 mM ammonium bicarbonate: acetonitrile (Honeywell, Burdick & Jackson, LC015-4) at ambient temperature. After 1h, the solution was replaced with 200 µl of acetonitrile and incubated until the gel slices turned opaque white. The acetonitrile was discarded and gel slices were further dried in a Speed Vac lyophilizer (Savant Instruments, Inc., SPD111V). Gel slices were rehydrated in 100 µl of 4 ng/µl of sequencing grade trypsin (Sigma, T6567) in 0.01% ProteaseMAX Surfactant (Promega, V2072) and 50 mM ammonium bicarbonate at 37°C for 18 hrs. The supernatant of each sample was reserved, and gel slices were further extracted with 200 µl of 80:20 (acetonitrile: 1% formic acid, (Millipore Sigma, 5.33002.0050). The supernatants were pooled and lyophilized.

LC/MS/MS analysis

Tryptic peptide digests were reconstituted in 25 µL 5% acetonitrile containing 0.1% (v/v) trifluoroacetic acid and separated on a NanoAcquity (Waters Corporation, Milford MA) UPLC. In brief, a 2.5 µL injection was loaded in 5% acetonitrile containing 0.1% formic acid at 4.0 µL/min for 4.0 min onto a 100 µm inside diameter (I.D.) fused-silica pre-column packed with 2 cm of 5 µm (200Å) Magic C18AQ (Bruker-Michrom, Auburn CA) and eluted using a gradient at 300 nL/min onto a 75 µm I.D. analytical column packed with 25 cm of 3 µm (100Å) Magic C18AQ particles to a gravity-pulled tip. The solvents were A: water (0.1% formic acid); and B: acetonitrile (0.1% formic acid). A linear gradient was developed from 5% solvent A to 35% solvent B in 60 minutes. Ions were introduced by positive electrospray ionization via liquid junction into a Q Exactive hybrid mass spectrometer (Thermo Scientific, Waltham MA). Mass spectra were acquired over *m/z* 300-1750 at 70,000 resolution (*m/z* 200) and data-dependent acquisition selected the top 10 most abundant precursor ions for tandem mass spectrometry by HCD fragmentation using an isolation width of 1.6 Da, collision energy of 27, and a resolution of 17,500.

MS data analysis

Raw data files were peak processed with Proteome Discoverer (version 2.1, Thermo) prior to database searching with Mascot Server (version 2.5) against the *Uniprot_Human*

database. Search parameters included trypsin specificity with two missed cleavages. The variable modifications of oxidized methionine, pyroglutamic acid for N-terminal glutamine, N-terminal acetylation of the protein, and a fixed modification for carbamidomethyl cysteine were considered. The mass tolerances were 10 ppm for the precursor and 0.05Da for the fragments. Scaffold Viewer (Proteome Software, Inc.) was used for peptide/ protein validation and label free quantitation. Using a protein threshold of 99%, a peptide threshold of 95%, and a minimum of two peptides per protein, identified peptides and spectral counts were exported and processed using SAINT on the crapome.org server with default settings (C(user);iter(2000,4000); LM=0,MF=0,Norm=1) (3). SAINT scores ≥ 0.8 are considered significant. The mass spectrometry proteomics data have been deposited to the ProteomeXchange Consortium via the PRIDE partner repository with the dataset identifier PXD015718.

Recombinant protein purification

Untagged PFN1 proteins were recombinantly expressed in *Escherichia coli* and purified using our established protocols, where PFN1 proteins either partitioned into the soluble fraction or into insoluble inclusion bodies (2). Here, PFN1 WT and G118V were purified from the soluble fraction, whereas PFN1 M114T and C71G were purified from the insoluble fraction. The GST-mDia1-FH1-FH2-C-His construct was obtained from Addgene (#85822) and purified as previously described (4). Protein concentration was measured spectrophotometrically for PFN1 as described (2), or with a Bicinchoninic Acid (BCA) kit (Thermo #23227) for mDia1.

Excited-state fluorescence decay kinetics measured by time-correlated single photon counting (PFN1 and formin binding studies)

For titration of labeled mDia1 with increasing concentrations of PFN1, recombinant GST-mDia1-FH1-FH2-$(His)_8$ was labeled with RED-Tris-NTA dye at a 3:2 protein:dye molar ratio according to the manufacturer's instructions (NanoTemper, MO-L018). A stock solution of [~1.5-2 mM] recombinant PFN1 protein in PBS was prepared by concentrating PFN1 with Amicon micro spin concentrators (3 kD MWCO, Millipore UFC500396) at 4°C and 10,000xg. Proteins were mixed together for each PFN1 titration point (twofold serial dilutions, ~1-4000 μM WT PFN1 and ~0.5-1000 μM M114T and G118V PFN1) and diluted as needed with PBS, resulting in a final concentration of 150 nM mDia1 and 100 nM RED-Tris-NTA dye at each point.

Excited-state fluorescence decay kinetics were obtained at each titration point using time-correlated single photon counting (TCSPC). Excitation at 445 nm was provided by the vertically polarized frequency-doubled output of a Titanium:sapphire laser (Coherent Mira 900D, Palo Alto, CA) that was pumped by a 10 W intracavity doubled diode laser (Coherent Verdi V10). The repetition rate of the 76 MHz pulse train was reduced to 3.8 MHz using an acousto-optic pulse picker. The sample was placed in a 20 μL synthetic fused silica cuvette (Starna, 16.12F-Q-1.5/Z15). The excitation was aligned into the cuvette without additional focusing and had approximately 50 μW of excitation power. Fluorescence was collected using a 35 mm focal length plano convex fused silica lens and passed through a Glan-Taylor polarizer oriented at the magic angle (54.7 degrees from vertical) to avoid any orientation bias in the lifetime measurements. The fluorescence was passed through a bandpass filter (Semrock 647/57) before being focused onto a PMC-100 photomultiplier tube (Becker-Hickl, Berlin, Germany). The output of the PMT was sent to a SPC-150 (Becker and Hickl) photon counting card along with a synchronization signal from a PHD-400 photodiode that recorded a pick-off from the pulse-picked Ti:sapphire beam. Photon counting rates were limited to $<8x10^4$ counts per second. For each sample 20 x 40 s acquisitions were performed and summed offline.

After intensity baseline correction, the first moments were calculated over an interval of 700 to 2000 channels (12.2 ps/channel). Because the first moment of RED-Tris-NTA increased only ~10% (from ~9.8 to 10.9 ns) upon binding, the first moment analysis provides an accurate model-free metric for monitoring the binding reaction.

The first moment values were adjusted to a baseline of 0 ns in the titration and fit using a single-site binding model:

$$R + L \rightleftharpoons LR$$

where the receptor-ligand complex concentration, [*LR*], is given by:

$$[LR] = \frac{\left(K_d + [R]_o + [L]_o + \sqrt{(K_d + [R]_o + [L]_o)^2 - 4[R]_o[L]_o}\right)}{2}$$

and $[L]_o$, is the total ligand concentration, $[R]_o$, the total receptor concentration and K_d, the dissociation constant, i.e., the ligand concentration at which half of receptors have bound ligand (5). Replicate binding data from different days were globally fit with the lifetime of each species and the K_d as global parameters. The labeled mDia1 concentration was fixed at the measured value of 0.15 μM. The first moment value for the complex, *RL*, was a local parameter for each replicate. All binding curves were scaled by the first moment value for the bound complex, *RL*, for overlay plots. Confidence intervals (95%) for K_d were estimated from the reduced chi-square (and subsequent F-test) surfaces generated from a rigorous error analysis (6). This error analysis takes into consideration correlation among all fit parameters. For example, the contribution of the incomplete saturation of the binding curve to the uncertainty is therefore explicitly considered. The Levenberg-Marquardt least-squares optimization algorithm implemented in Savuka was used for the global analysis and error analysis and can be downloaded at www.osmanbilsel.com (7).

Profilin Tryptophan Quenching

Profilin's intrinsic Tryptophan fluorescence (excitation wavelength = 295 nm, emission wavelength = 325 nm) was recorded using a fluorometer (PTI QuantaMaster, Horiba). Titration of 1 μM profilin by the first poly-proline track of mDia1 FH1 (sequence PPPPPFGFGVPAAPVL) was performed by sequentially adding small amounts of poly-proline (total volume increase was kept lower than 2%) in the quartz cuvette (light path = 10 mm). The peptide was dissolved in the final assay buffer: 5 mM Tris HCl pH7.4, 1 mM MgCl2, 200 μM EGTA, 200 μM ATP, 10 mM DTT and 50 mM KCl at a stock concentration of 300 μM. For each profilin variant, data was obtained from three independent repetitions, and the normalized fluorescence intensities were fitted by a quadratic function to derive the affinity constant.

***In vitro* actin polymerization assays with recombinant protein**

Measurement of mDia1 formin-induced actin filament polymerization rate was performed using a microfluidics device paired to a microscopy setup, as described (8, 9). Briefly, a polydimethylsiloxane (PDMS, Sylgard) chamber, 20 μm in height, was mounted on a cleaned coverslip. The three inlets and the outlet were connected to pressure-controlled tubes (MFCS, Fluigent) filled with solutions of different bio-chemical compositions. The microfluidics chamber was functionalized with spectrin seeds before extensive BSA surface passivation. Actin filaments were elongated from seed upon exposure to monomeric actin (10% Alexa488-labelled on surface Lysines) in F-buffer (5 mM Tris HCl pH 7.4, 50 mM KCl, 1 mM $MgCl_2$,0.2 mM EGTA, 0.2 mM ATP, 10 mM DTT and 1 mM DABCO) at 25°C (microscope objective temperature controller from OkoLab, Italy). mDia1 formins were bound to filament barbed ends by exposing the latter to a 10 nM mDia1

solution for 20 seconds. For a direct comparison of the impact of PFN variants on formin-induced barbed end polymerization rate and mDia1 processivity, the chamber was half exposed to a solution containing 1 μM actin and a fixed concentraiton of PFN WT while the other half was exposed to a solution containing 1 μM actin and the same concentration of PFN C71G or G118V.

The microfluidic setup was placed on a Nikon TiE inverted microscope, equipped with a 60x oil-immersion objective, and controlled with Micromanager. Filaments were illuminated using a 100 mW tunable laser in TIRF mode (iLAS2, Roper Scientific), and images were acquired with a sCMOS Orca-Flash 4.0 V2+ camera (Hamamatsu). Images were analyzed using the ImageJ software to measure filament elongation rates. Changes from fast to slow polymerization velocities were counted as formin dissociation events. The survival fraction of formin elongating filaments as a function of time was reconstructed and data were fitted with a single exponential $f=\exp(-t \cdot k_{off})$, where k_{off} is the dissociation rate of formin from the barbed end, using a Levenberg-Marquardt algorithm through least square fitting (from the 'scipy' package in python). The log-rank test from the Kaplan-Meier estimator (from the 'lifelines' python package) was used to measure the statistical significant difference between survival functions.

IMM-01-induced actin polymerization in cells

Cells ($1.5x10^5$) were plated on coverslips and V5-PFN1 expression was induced for 24 hours. After induction, the cells were maintained in growth media modified with 0.05% fetal bovine serum during 18 hours and, consecutively, treated with 0.027% dimethyl sulfoxide (DMSO, Sigma-Aldrich, D2650) or 10μM IMM-01 (Sigma-Aldrich, SML1064) for 30 minutes, 1 and 4 hours as indicated. Immunofluorescence analysis was performed as mentioned before. To observed F-actin structures, Alexa Fluor 546-conjugated Phalloidin (Invitrogen, A22281) was used after secondary antibody incubation for 45 min following the manufacture's recommendations. For image analysis, stacked images were deconvolved using the LAS AF One Software Blind algorithm (10 iterations). Maximum projections were created from deconvolved stacks for downstream quantification. Six fields of view per condition were analyzed in a blinded manner to manually count the number of cells that showed stress-fiber like structures using Cell Counter plugin (Fiji, ImageJ). The total number of cells per field of view was determined similarly. The sum of the number of cells in all the analyzed field of view was used to calculate the percentage for each sample condition. The assay was repeated for three independent biological experiments and a total of 300-450 cells were analyzed per sample condition among all experiments.

Pyrene-actin assembly assay

Spontaneous actin assembly assays were performed using the change in fluorescence of 5% pyrenyl-labeled actin (excitation wavelength = 366 nm, emission wavelength = 407 nm) in G buffer (5 mM Tris/HCl, pH 7.4, 0.2 mM ATP, 0.1 mM $CaCl_2$, 1mM DTT) supplemented with 1 mM $MgCl_2$, 0.2 mM EGTA, and 50 mM KCl. The polymerization was conducted with 1.5 μM actin and 3 μM Profilin 1 WT and ALS mutants, in the presence of 5 nM of dimeric SNAP-mDia1(FH1FH2DAD)-6xHis. All experiments were carried out at 20 °C in a Safas Xenius FLX spectrofluorimeter (Safas, Monaco), the pyrene fluorescence of each sample being recorded every 12 seconds. Simulation of pyrene actin assembly was achieved by using the model described by Paul and Pollard located at https://vcell.org/ (10-12).

Molecular dynamics simulations

Molecular dynamics simulations were performed with NAMD 2.13 (13) using the CHARMM 27 force field (14). The x-ray structures of PFN1 WT (PDB code 4X1L) and M114T mutant (PDB code 4X25) served as the starting configurations in the MD simulations of the two PFN1 variants. The human PFN1 NMR structure (PDB code 1PFL) was used to model missing loop residues 92-96 (WT) and 93-97 (M114T). The x-ray structure of PFN1 M114T was used to model missing loop residues 57-62 in PFN1 WT. In the MD simulations of G118V and C71G mutant PFN1, the initial structures were generated from the x-ray structure of WT PFN1 with added loops and after mutation of Gly118 to Val and Cys71 to Gly (respectively) performed using the Mutator plug-in of the Visual Molecular Dynamics program (15). The initial structures of the three PFN1 variants were solvated in a TIP3P water box and neutralized by adding two chloride ions. The solvated structures were minimized using the conjugate gradient method followed by random assignment of particle velocities from the Maxwell distribution and equilibration in the isothermal-isobaric ensemble. The pressure and temperature were maintained at 1 atm and 298 K using Langevin dynamics and the Nosé-Hoover Langevin piston method. The SHAKE constraint algorithm was used to allow a 2 fs time step (16). The particle mesh Ewald method was used to calculate electrostatic interactions with periodic boundary conditions. After equilibration in the isothermal-isobaric ensemble, final temperature equilibration was performed in the microcanonical ensemble for five independent trajectories with velocity reassignment to ensure temperature stabilization around 298 K. After these thermal equilibration steps, 100 ns of structural equilibration was performed in the microcanonical ensemble followed by an additional 220 ns of data collection for analysis.

Network analysis

Network analysis was performed by the bio3d package in the R environment (R development core team, 2006; http://www.R-project.org) using cross-correlations calculated after alignment on all residues (17). Cross-correlations were included in the calculations with a threshold of 0.5 and community membership was determined using the greedy algorithm (18).

Network graphs overlaid on the structure represent each community by a sphere located at the geometric center of each community. The community radius (R_i) and edge weight between two communities (E_{ij}) are defined as

$$R_i = \frac{\sqrt{N_i}}{3}$$

$$E_{ij} = \frac{-ln\left|\max\left(C_{ij}\right)\right|}{4},$$

where N_i is the number of residues in each community and max(C_{ij}) is the maximum correlation coefficient between residues in each connected pair of communities. The scaling was chosen to illustrate relative differences between communities without obscuring the underlying structure. Residues of the structure are colored according to community membership with unconnected communities in white. The number of shortest paths that pass through each node (betweenness) was calculated from the full network defined by the underlying cross-correlation matrix (where each residue is a node).

Interfacial residues

Actin and Poly-Pro binding residues were identified by calculating the solvent accessible surface area (SASA) for each residue of PFN1 in the presence and absence of actin and Poly-Pro using the X-ray structure of the ternary complex (PDB code: 2PAV). The SASA

was measured using the implementation in VMD (15, 19). Residues with a difference > 1 $Å^2$ in the SASA measured with and without the shielding from actin/ Poly-Pro were defined as interfacial residues. The Poly-Pro binding residues identified by this method are: 4, 6-7, 10, 30, 32, 108, 130-131, 134-135, 138, and 140. The actin binding residues identified by this method are: 60-63, 70, 72-75, 81-83, 85, 87, 89-91, 98, 100, 118-123, 125-126, and 129-130. E130 is identified as an interfacial residue for both actin and Poly-Pro; where residues are labeled by interface, E130 is defined as an actin interfacial residue because the buried surface area with actin is greater than the buried surface area with Poly-Pro (7.3 $Å^2$ for actin, 1.7 $Å^2$ for Poly-Pro). The binding surface area (BSA) calculated in the MD simulation trajectories is defined as the SASA of the subset of residues that form the binding interface with actin or Poly-Pro.

Quantification of Structural Fluctuations

The dihedral angles, secondary structure probabilities, hydrogen bonds, and root mean square fluctuations (RMSF) were calculated by the implementations in VMD (15). Dihedral angles are defined in the range of (-180°, 180°) and were corrected to minimize artificial transitions at the boundary which affect the standard deviation. The secondary structure probabilities were calculated using the STRIDE method (20). A hydrogen bond is defined as present when the donor-hydrogen-acceptor angle is 130° < θ < 180° and the donor-acceptor distance is less than 3.5 Å. The RMSF is the average positional fluctuation over the length of the trajectory (T). The RMSF was calculated for the Cα atom of each residue using the position (r_i) in the first frame of the equilibrated trajectories (t_0) as the reference conformation according to the equation:

$$RMSF_i = \left[\frac{1}{T}\sum_{t_j=1}^{T}\left|r_i(t_j) - r_i(t_0)\right|^2\right]^{1/2}.$$

Biochemical fractionation of V5-PFN1 HeLa lysates under proteostatic stress

HeLa cells were plated in 12 well plates at a density of 10^6 cells per plate. Cells were induced at 24 hours with 1 µg/ml doxycycline and simultaneously treated with drug (MG132 (Sigma 474787), 3-MA (Sigma M-9281), leupeptin (Sigma L9783), epoxomicin (Sigma E3652), chloroquine (Sigma C6628)) or vehicle. At 48 hours cells were washed with PBS and lysed for 15 minutes in 160 µL buffer (25 mM HEPES, 25 mM KCl, 5 mM EDTA (Fisher; E478-500), 1% NP-40 (MP Biomedicals; 198596), and 10% v/v glycerol (Acros; 15982–0010) in water; pH 7.0). Cells were scraped and spun at 15890 x g for 10 minutes at 4°C. The supernatant was reserved as the soluble fraction and the pellet was washed with one volume PBS, spun again, decanted, and resuspended in one volume 8M urea.

Human Lymphoblast cell culture experiments

Six control and five C71G PFN1-mutant patient-derived lymphoblast cell lines were cultured in T-25 suspension flasks (Grein Bio-One, 690190) and maintained using Roswell Park Memorial Institute (RPMI) 1640 Medium (Invitrogen, 11875119) supplemented with 15% (vol/vol) heat-inactivated fetal bovine serum (Sigma-Aldrich, F-4135) and 1% (wt/vol) penicillin and streptomycin. Half of the medium was changed every 3 days and the cells were divided when confluent.

When lymphoblast cultures reached confluency, cells were collected by centrifugation and lysed using RIPA Buffer (Boston BioProducts, 115-500) supplemented with protease inhibitors (Roche 11836170001). The lysates were processed for Western blot analysis as described above. Similarly, total RNA was isolated using Trizol (Invitrogen, 15596026). cDNA was synthesized using iScript Reverse Transcription Supermix (Biorad,

170-8840) according to the manufacturer's instructions. Quantitative real-time PCR (qPCR) was performed using 25ng of RNA, *PFN1* primers (Biorad, qHsaCED0057302), and 5x iTaq Universal SYBR Green Supermix (Biorad, 172-5120). *GAPDH* was amplified as internal control. The qPCR was conducted at 95 °C for 2 min, 40 cycles of 95 °C for 5s and 60 °C for 30s, and a melt-curve of 65–95 °C (0.5 °C increments per 5 s). The relative gene expression was determined using the ΔΔCT method and normalized to the internal control. Experiments were performed using CFX384 Touch Real-Time PCR Detection System (Biorad). Samples were run in triplicate per experiment, and the gene-expression data is reported as an average of at least two independent biological experiments per cell line.

Statistical analysis

At least three independent experiments were performed for data with statistical analyses. Statistical analyses were calculated using GraphPad Prism v8.1.2. Statistical tests are stated in the figure legends.

Supplementary text: Extended analysis of the MD trajectories

We used network theory to analyze our MD simulations of PFN1 WT, M114T and G118V (21). Using this approach, we identified for each system, a network describing the internal dynamics of PFN1 with communities of residues whose dynamics are correlated. We observed that the C-terminal helix (α_4, residues 121-138 see **fig. 3** and **SI Appendix fig. S6**) is the only community that contains residues that are part of the binding interface with both actin and Poly-Pro. The fragmentation of this helix into two communities in the mutants occurs at the division between the two interfaces (**fig. 3** and **SI Appendix fig. S6**). The fragmentation of the community corresponds to increased structural fluctuations in this region as shown by the root mean square fluctuations (RMSF) (**SI Appendix fig. S7A**). The change in the internal dynamics is not isolated to this helix - the RMSF for most residues is increased in the mutants compared to the WT, especially for the Poly-Pro binding interface in G118V (**SI Appendix fig. S7A, top**).

The fluctuations of the backbone dihedral angles show localized changes more closely related to the mutations. In G118V (**SI Appendix fig. S7B, blue**), the loops between β6/β7 and β7/α4 have increased standard deviation due to sampling a broader range of conformations. While these residues are in loop regions, these turns have very low backbone dihedral fluctuations in the WT and M114T variants (**SI Appendix fig. S7B, green/orange**). The hydrogen bond probability between K108 (β6/β7 turn) and Y140 (α4 terminus) form a less stable hydrogen bond in G118V (WT K108-Y140 H-bond probability = 0.82, M114T p = 0.88, G118V p = 0.64), consistent with the increased dihedral angle fluctuations and RMSF of these Poly-Pro interfacial residues (**SI Appendix fig. S7A, B**).

The backbone dihedral angle fluctuations in M114T are affected nearer the N-terminal end (β1, β2/α1 loop) (**SI Appendix fig. S7B, orange**). The affected residues of β1 (Q18/D19) H-bond with both K38 (β2/α1 loop) and M/T114 and these H-bonds are altered in the M114T variant. The side chain of K38 shows increased H-bond probabilities with Q18 and D19 in M114T which may help limit the sampling of alternate dihedral angle conformations by G37/K38 compared to WT and G118V (WT Q18/D19-K38 H-bond p = 0.20/0.33, M114T p = 0.29/0.53, G118V p = 0.11/0.15). Q18 and D19 also form primarily backbone H-bonds with M/T114. These H-bonds show small perturbations (changes of ± 0.10 in the H-bond probability) with the M114T mutation that result in conformational transitions in the backbone dihedral angles of Q18/D19 in M114T that are not observed in the trajectories of the WT or G118V. These results suggest that the dynamics of the β-strands near T114 are altered by the mutation, consistent with the change in the community network (**SI Appendix fig. S6**).

There are larger fluctuations (i.e., larger standard deviations) in the surface areas of PFN1 that bind actin and Poly-Pro in the mutants (**SI Appendix fig. S7C**). Despite these changes in the internal dynamics, the secondary structure probabilities are not altered in the mutant PFN1 proteins (**SI Appendix fig. S7D**). However, a structural rearrangement is predicted for G118V in the ternary complex. G118 is located on the surface of PFN1 and interacts with actin. For this reason, the G118V mutation directly affects the actin binding surface. It increases the average binding surface area by approximately 41 $Å^2$ because of the larger solvent exposed side chain (**SI Appendix fig. S7C**). In addition, when the structure of the G118V mutant is aligned with that of PFN1 in the crystal structure of the ternary complex (pdb ID 2PAV), V118 has a steric clash with T351 and Q354 of actin (**SI Appendix fig. S8**). This result suggests that a structural rearrangement of PFN1 and actin in the complex is necessary to allow binding.

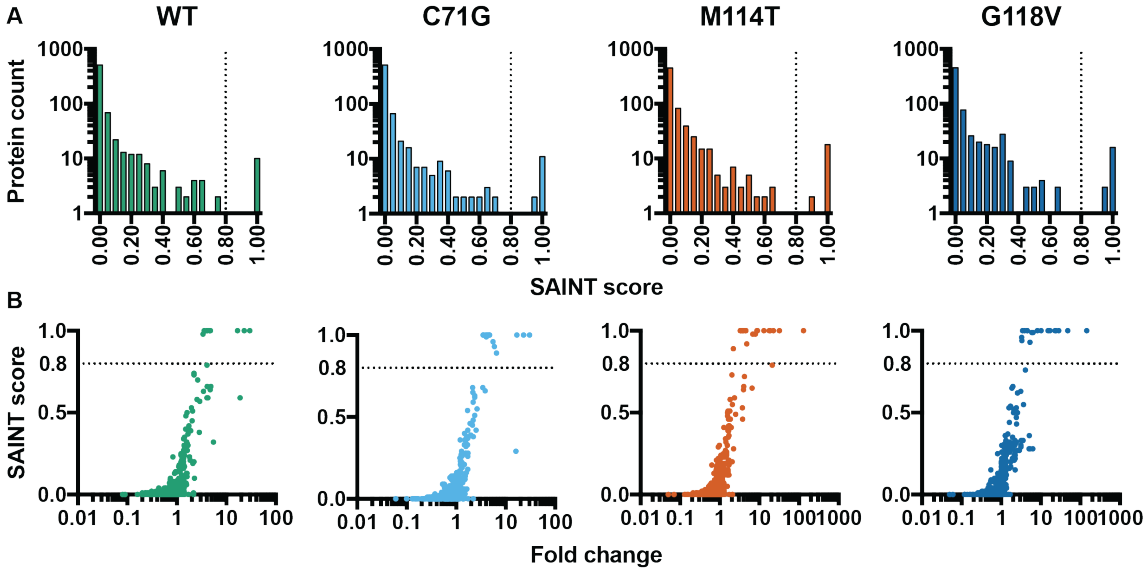

Figure S1. Distribution of SAINT scores and fold change for PFN1 interactors from mass spectrometry data. (A) Histogram of SAINT scores for the indicated variant versus the V5 negative control. Most scores are low (>90% are below 0.5), with a peak at 0 and a tail extending to approximately 0.7. This distribution represents nonspecific interactions. The dotted line at 0.8 denotes the cut-off used in this study, where all SAINT scores ≥0.8 were considered high confidence. A second peak in the distribution is centered on the maximum SAINT score of 1. **(B)** SAINT scores correlate positively with fold change enrichment. For each variant, the mean fold change (FC) enrichment calculated by SAINT is plotted against SAINT score for each protein in the data set. Each point represents all replicates of a single protein. Both (A) and (B) reflect all three replicates of IP-MS.

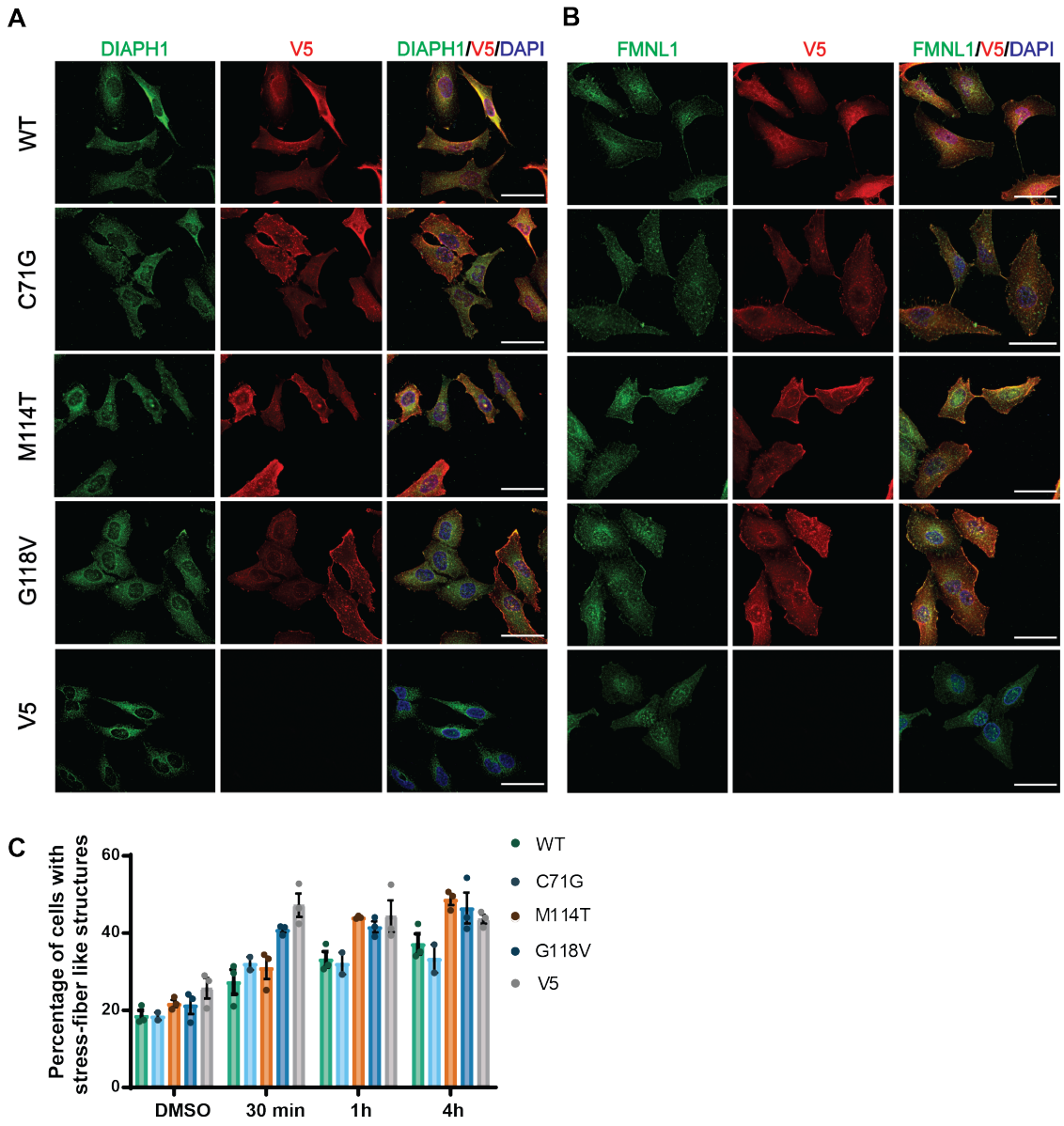

Figure S2. Additional analyses of formin proteins in V5-PFN1 HeLa cell lines. (A-B) Immunofluorescence analyses of formin protein Diaph1 (A) or FMNL1 (B) together with V5-PFN1 in stable HeLa cell lines indicates there are no qualitative differences in intensity or localization of these markers across cell lines expressing different PFN1 variants. We note that there is some heterogeneity in the staining patterns for these markers in each field of view. However, repeated and blinded analyses did not uncover robust or quantifiable differences between PFN1 lines. Scale bar = 50μm. (**C**) Bar graph showing percentages of cells with stress-fiber like structures after treatment with IMM-01, an activator of DIAPH1/2 proteins, as described in the main text Figure 2.

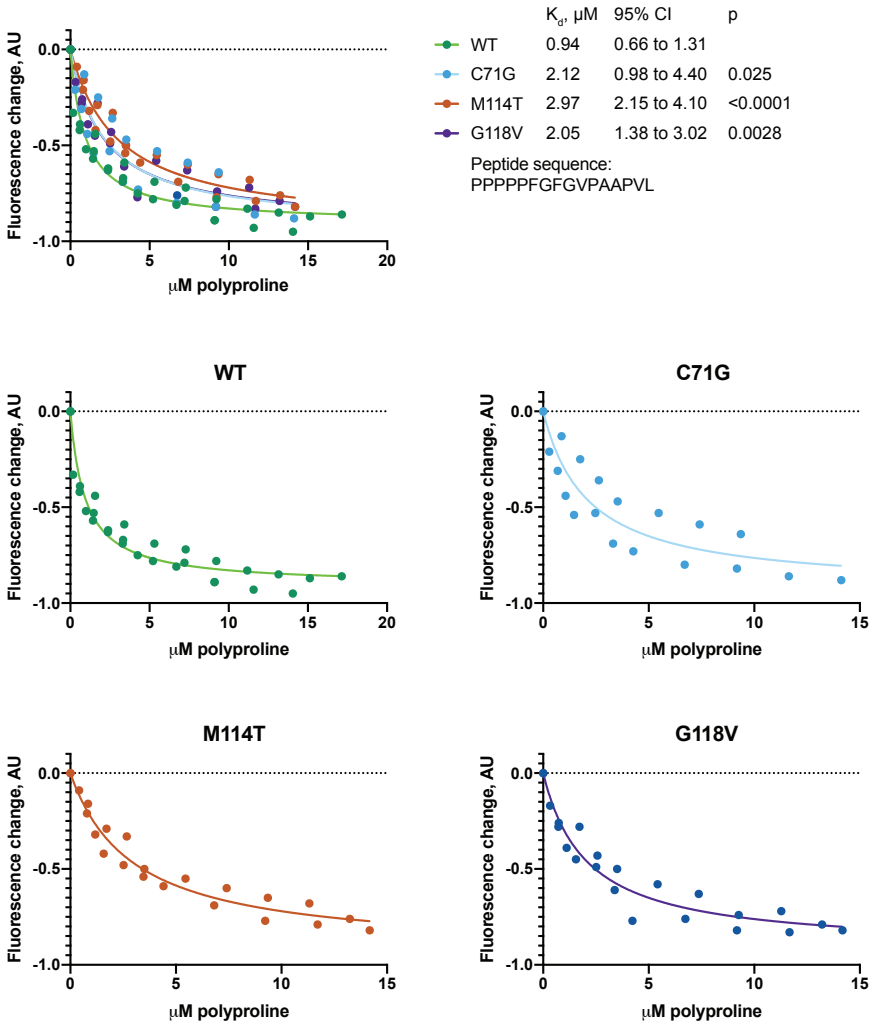

Figure S3. Binding of PFN1 variants to a poly-Pro sequence derived from mDia1. **(A)** The poly-Pro sequence from the FH1 domain of mDia1 (adjacent to the FH2 domain; PPPPPFGFGVPAAPVL) was titrated with the indicated PFN1 variant. Binding is detected as a change in the intrinsic PFN1 tryptophan fluorescence. The table shows the dissociation constant (K_d) with 95% confidence intervals (CI) as well as p values for extra-sum-of-squares F test for difference from WT. **(B-E)** The individual binding curves are shown for each PFN1 variant.

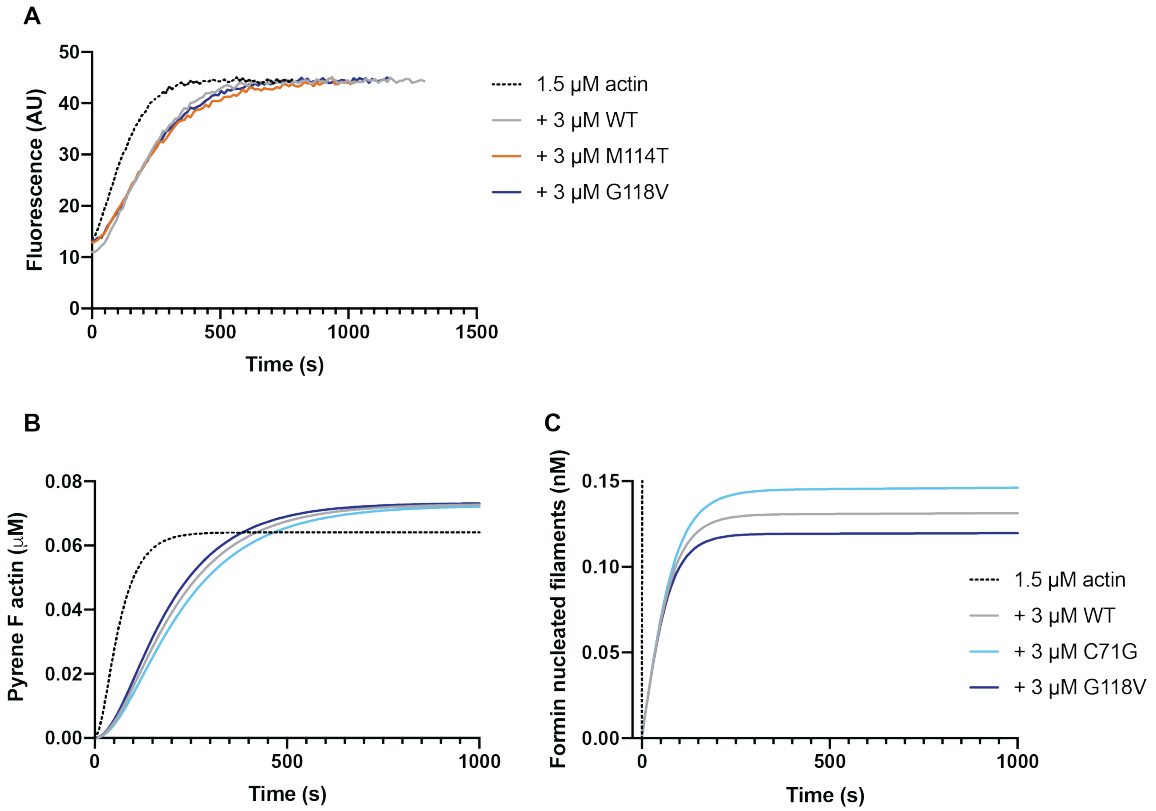

Figure S4. Experimental and modeling analyses of bulk pyrene actin assembly assays. (**A**) Bulk pyrene actin assembly assays conducted in the presence of 1.5 µM actin (5% pyrene labelled), 5 nM mDia1 and 0 or 3 µM of PFN1 variants show no appreciable differences in fluorescence signals arising from polymerized actin in the presence of the different profilin variants. (**B-C**) Simulation of pyrene actin assembly using the elongation rates from Figure 2B and the model described by Paul and Pollard located at https://vcell.org/ (with modifications highlighted in Dataset S3) (10-12). (B) Changes in Pyrene F actin signal as a function of time is predicted to be similar for the three PFN1 variants exhibiting different maximum elongation rates (from Figure 2B). The output file used to generate this plot is in Dataset S3. (C) The outcomes of the model indicate differences in the number of formin-nucleated actin filaments amongst the PFN1 variants (output file is in Dataset S3) that appear to inversely correlate with rates of actin elongation (from Figure 2B). Results of these simulations indicate that differences in formin-mediated nucleation activity can offset rates of actin elongation in the pyrene assembly assay.

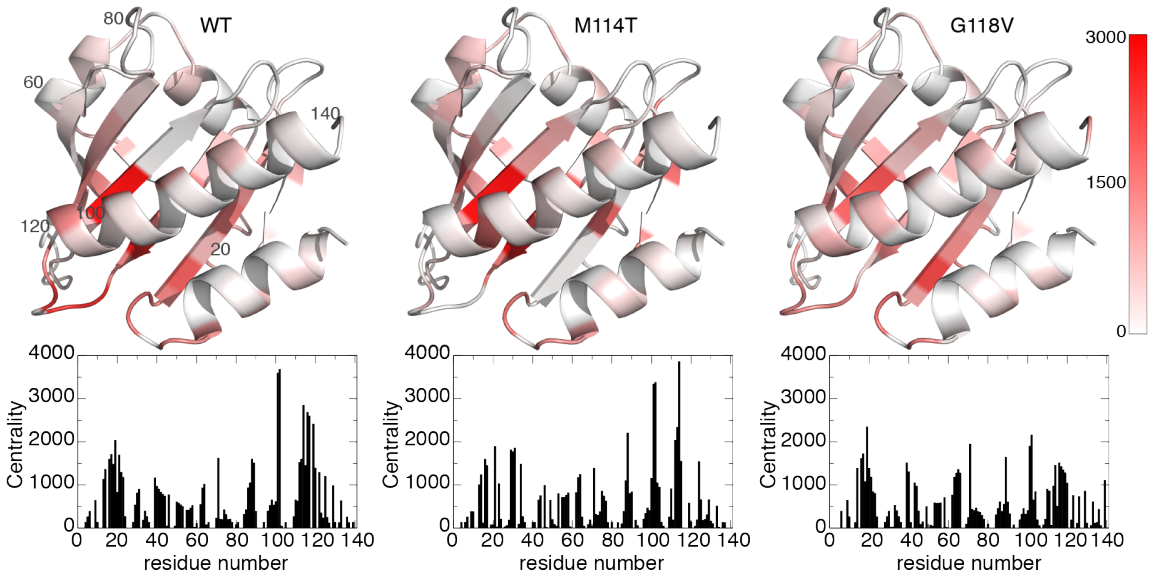

Figure S5. Betweenness centrality determined from network analysis of molecular dynamics simulations for PFN1 variants. Results reveal differences in the topology of the molecular dynamics correlation networks between WT, M114T and G118V. Betweenness centrality measured for each residue, defined as the number of unique-shortest paths crossing that residue, is mapped on the structures of PFN1 (top) and as a function of the residue number (bottom).

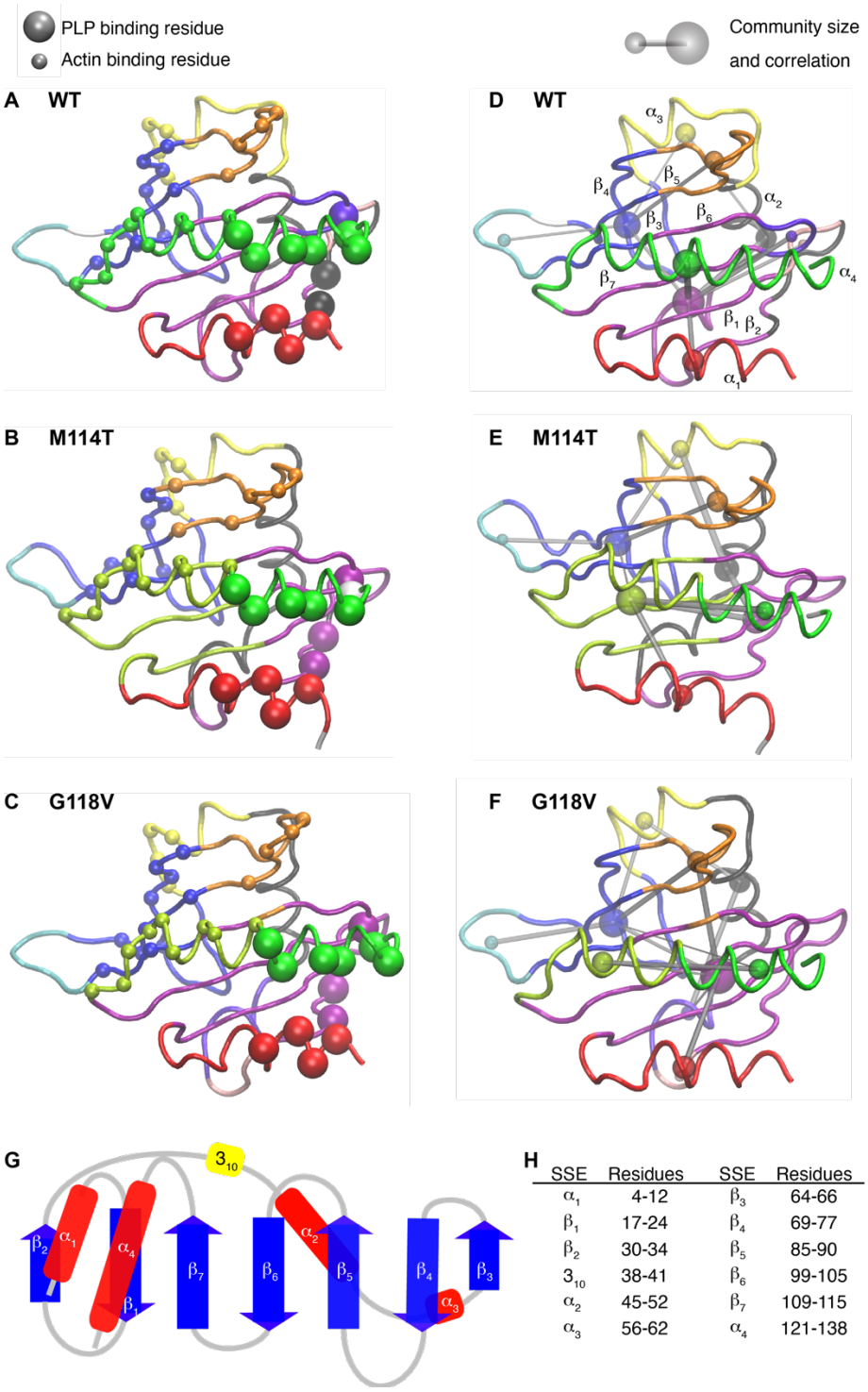

SSE	Residues	SSE	Residues
α_1	4-12	β_3	64-66
β_1	17-24	β_4	69-77
β_2	30-34	β_5	85-90
3_{10}	38-41	β_6	99-105
α_2	45-52	β_7	109-115
α_3	56-62	α_4	121-138

Figure S6. ALS-linked mutations alter the communities of residues within PFN1 that exhibit correlated dynamics. Community analysis of the networks observed for WT **(A, D)**, M114T **(B, E)** and G118V **(C, F)** PFN1 variants. Distinct communities are represented

in different colors, and residues are colored according to their community membership. The location of actin and Poly-Pro binding residues is shown in **A**, **B** and **C**. Poly-Pro interfacial residues are shown as large spheres and actin interfacial residues are shown as small spheres (key: light gray spheres). Interfacial residues are residues with buried surface area of > 1 $Å^2$ in the crystal structure of the ternary complex (PDB code: 2PAV). The C-terminal helix (α_4, residues 121-138) is the only community that contains residues that are part of the binding interface with both actin and Poly-Pro. For M114T and G118V, a fragmentation of this helix into two communities is observed at the division between the two interfaces (i.e., note the transition between small and large spheres). In **D**, **E** and **F** spheres are proportional to the size of each community and the width of the lines is proportional to the strength of the correlation between communities. A schematic representation of the secondary structure of PFN1 is shown in **G**. The location of each secondary structural element (SSE) is shown in **H**. Additional information for this figure can be found in the Supplementary text (extended analysis of the MD trajectories).

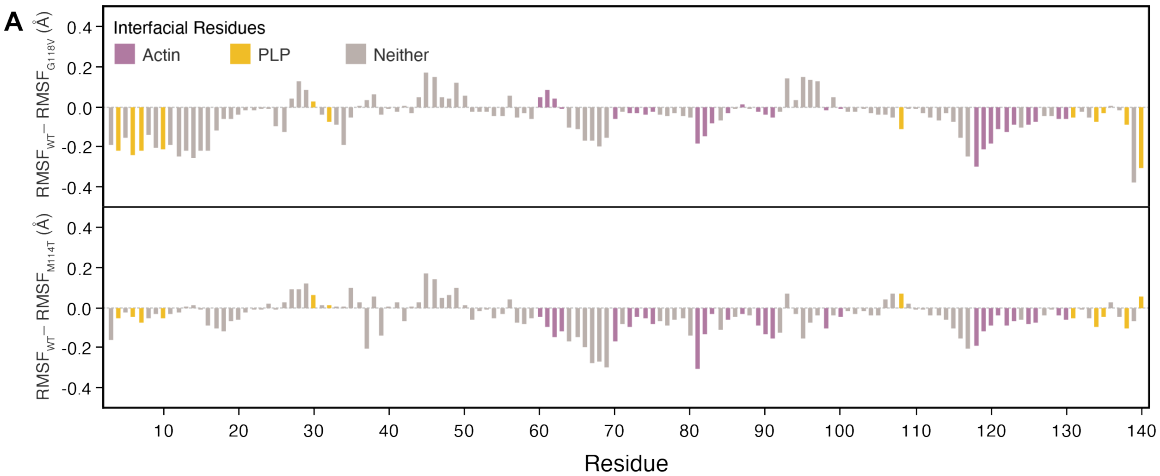

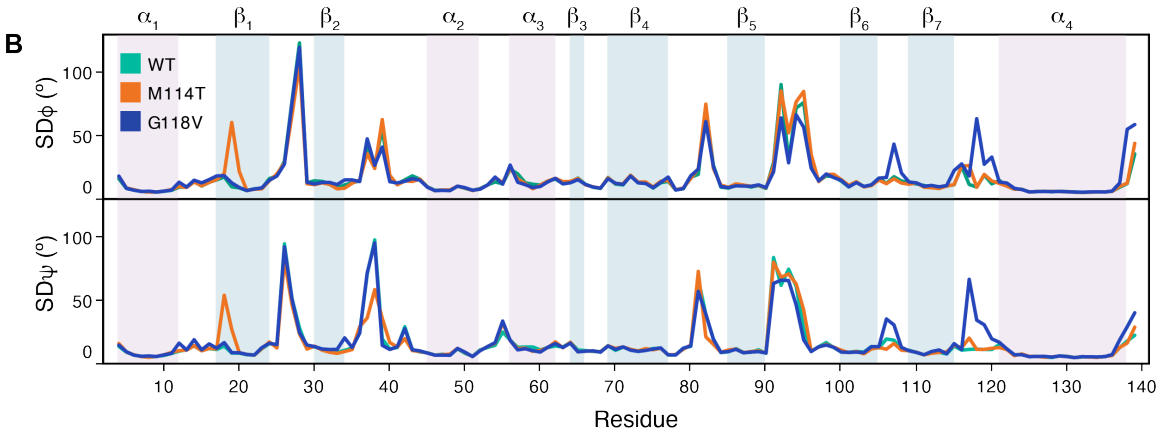

C

	Actin BSA (Å²)	PLP BSA (Å²)
WT	2,189 ± 23	882 ± 27
M114T	2,219 ± 55	891 ± 35
G118V	2,230 ± 37	899 ± 43

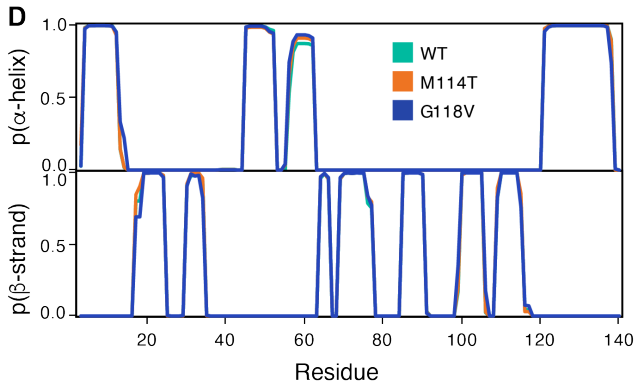

Figure S7. Analysis of the MD simulations of PFN1 variants shows that ALS-linked mutations increase the flexibility without altering the structure of PFN1. (A) Difference in RMSF of Cα atoms between WT and mutants is shown for M114T (bottom) and G118V (top) identifies residues with changes in internal dynamics. Interfacial residues are highlighted in purple for actin and yellow for Poly-Pro. Changes in internal dynamics are not only detected in the C-terminal helix (α_4, residues 121-138), where there is fragmentation of this community in the mutants (**SI Appendix fig. S6**), but most residues exhibit increased internal dynamics in the mutants compared to the WT, especially for the Poly-Pro binding (PLP; yellow) interface within G118V (top). **(B)** Standard deviation of the φ and ψ backbone dihedral angles for WT (green), M114T (orange) and G118V (blue). Secondary structure is marked with colored bands: α-helices in pink and β-strands in blue. **(C)** Mean and standard deviation across trajectories of the actin/Poly-Pro binding surface

area (BSA) of WT PFN1 and M114T/G118V mutants. BSA is defined as the combined surface area of the residues in the binding interface. The standard deviations increase for the mutants, indicative of greater fluctuation. **(D)** Despite changes in the internal dynamics of ALS-linked PFN1 variants, secondary structure probabilities for α-helices and β-strands are similar for WT (green), M114T (orange) and G118V (blue). Additional information for this figure can be found in the Supplementary text (extended analysis of the MD trajectories).

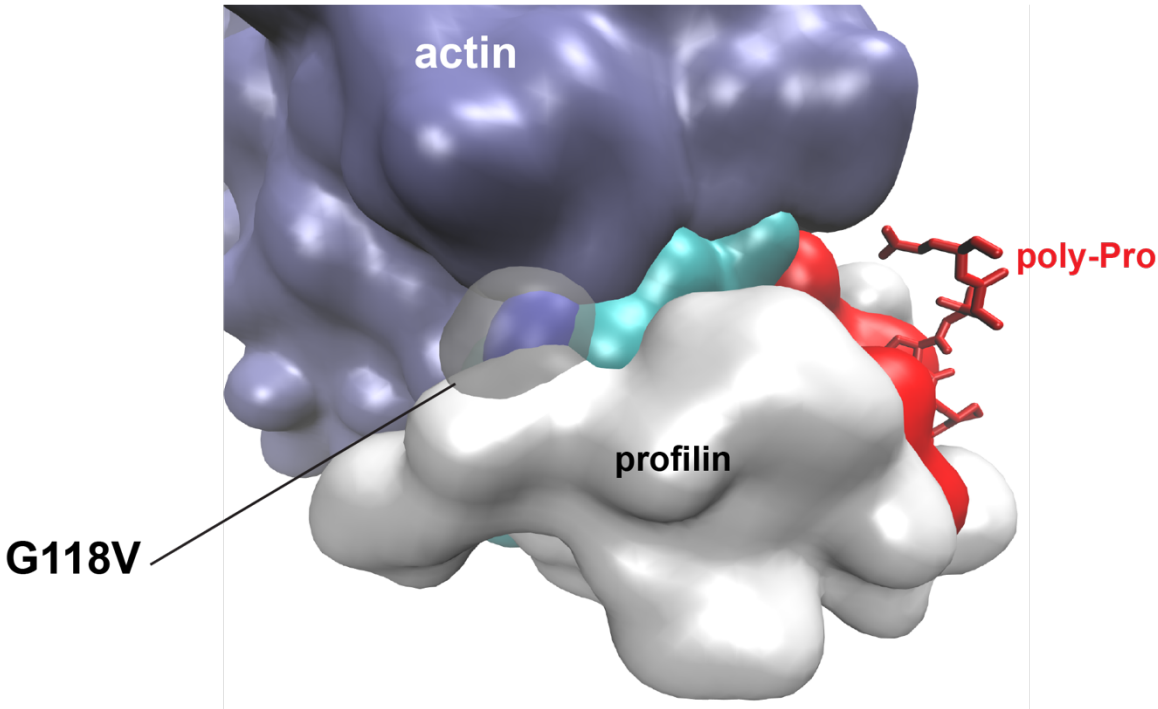

Figure S8: **Effect of the G118V mutation on the actin binding interface of PFN1.** The effect of G118V mutation on the binding surface is modeled using the crystal structure of the PFN1/actin/Poly-Pro ternary complex (PDB code: 2PAV). PFN1 is shown in white/gray, actin in purple, and poly-Pro as red sticks. The Poly-Pro interfacial region is highlighted as a red surface on the PFN1 protein, whereas the actin interfacial region is highlighted in cyan on the PFN1 protein. The structure of V118 from the G118V PFN1 MD simulations is overlayed and depicted as a transparent gray surface (labeled) with the surface in blue underneath. This representation indicates a steric clash between PFN1 G118V (i.e., the valine residue) with actin, implicating that a structural rearrangement of PFN1 and actin in the complex is necessary to allow binding. Additional information for this figure can be found in the Supplementary text (extended analysis of the MD trajectories).

Legends for Supplemental Dataset 1. Mass Spectrometry Data

Tab 1. Spectral count values for all proteins detected in IP-MS experiments. This table shows the total spectral counts, or total number of peptides derived from a particular protein, that are detected by the MS instrument. These values are shown for all proteins detected in each of three MS-IP replicates for each cell line. Proteins are ranked by sum of total abundance in all V5-PFN1 samples, and bars represent the abundance compared to the most abundant protein in all experiments.

Tab 2. SAINT scores versus V5 for all proteins detected in IP-MS experiments. Shown are the results of SAINT analysis with V5 as the negative control: the SAINT scores for all proteins detected, by PFN1 variant, as well as the fold change relative to V5 calculated by SAINT using spectral counts. Proteins are ranked by maximum SAINT score, and bars represent the SAINT score.

Tab 3. iBAQ values for all proteins detected in IP-MS experiments. This table shows the iBAQ values for all proteins detected in each of three independent IP-MS experiments for each of the five cell lines. The iBAQ value reports on the abundance of each peptide (and thus, protein). For every peptide that is detected, the area under the peptide peak (the peak area) in the mass chromatogram is determined. This peak area is then normalized to the molecular weight of the protein. Therefore, iBAQ scores are a quantitative measure of protein abundance and reflect the sum of all detected peptides from a protein, divided by the number of unique peptides predicted from the protein sequence. This normalizes for large proteins, which would otherwise be overrepresented (22, 23). In this tab, proteins are ranked by sum of iBAQ scores in all V5-PFN1 samples, and orange bars represent the abundance compared to the most abundant protein in all experiments.

Tab 4. iBAQ values for proteins that are enriched in PFN1 IP-MS experiments. This tab lists the 28 proteins that were detected with at least fourfold enrichment in iBAQ value over the V5-only negative control line from the data listed in Tab 5. The table shows all proteins that are enriched over V5-only in at least one cell line, i.e. if the iBAQ score is at least fourfold higher than V5 in all three replicates in Tab 5. For each cell line the mean iBAQ score is reported, as well as the number of individual IP-MS replicates showing enrichment. The fold-change over V5 is indicated for each protein. The table is sorted by abundance, then by total replicates enriched among all lines. For proteins that were not detected in the V5-only, the fold-enrichment was assigned as >100 as a conservative lower limit. The majority of proteins on this list of 28 are the same as those 21 proteins identified through the SAINT analysis; compare the proteins in Figure 1B of the main text with the proteins in this tab (proteins are color coded the same in both).

Tab 5. SAINT scores versus WT for all proteins detected in IP-MS experiments. Shown are the results of SAINT analysis with WT as the negative control: the SAINT scores for all proteins detected, by PFN1 variant, as well as the fold change relative to WT calculated by SAINT using spectral counts. Proteins are ranked by maximum SAINT score, and bars represent the SAINT score.

Tab 6. Gene Ontology terms, all significantly enriched. STRING was used to identify enriched GO terms for the set of proteins with SAINT score versus WT ≥ 0.8 with any

PFN1 variant. This table shows all GO terms with FDR < 0.05, term description, the count of each term in the set and in the genome, the term FDR, and the identities of each protein matching the term. Terms are divided into categories of component, process, and function.

Legends for Supplemental Dataset 2. Time-correlated single photon counting (TCSPC) data

Tab 1. Raw data from the TCSPC experiment. Values in a column "x" refer to the PFN1 concentration (μM). Values in a column "y" refer to the change in fluorescence lifetime (ns). There are three data sets for WT, and two each for G118V and M114T.

Tab 2. Results of the global fitting and error analyses for PFN1 WT and GST-mDia1-FH1-FH2-$(His)_8$ as described above in the Methods under "Excited-state fluorescence decay kinetics measured by time-correlated single photon counting (PFN1 and formin binding studies)".

Tab 3. Same as Tab 2 for PFN1 M114T.

Tab 4. Same as Tab 2 for PFN1 G118V.

Tab 5. Enlarged graph for PFN1 WT, M114T and G118V binding data.

Legends for Supplemental Dataset 3. Use of computational methods to simulate actin polymerization and formin-induced nucleation of filaments as a function of PFN1 variant.

Tab 1. VCell parameters. The model developed by Paul and Pollard was accessed through https://vcell.org/ and used to simulate the process of actin elongation in the pyrene assembly assay (10-12). The parameters and default values in the model are from Paul and Pollard (11). Parameters that were changed to account for mDia1 used herein versus yeast Bni1p in the original report are highlighted in yellow.

Tab 2. Pyrene F-actin. Output file for the simulation described in Tab 1 for each variant. Data is plotted in **Figure S4B**.

Tab 3. Number of ends-nucleated by formin. Output file for the simulation described in Tab 1 for each variant. Data is plotted in **Figure S4C**.

Supplemental Video 1. Actin elongation in the presence of different PFN1 variants. mDia1 processivity and formin-induced filament barbed end elongation rates were assayed in a microfluidics assay (flow from left to right; illustrated in Figure 2A). Filament barbed end, initially exposed to mDia1, elongates from surface anchored spectrin-actin seeds, in the presence of 1 μM actin (10% alexa488-labelled) and 0.5 μM WT (left), C71G (middle) or G118V (right) PFN1 variants. Scale bar: 10 μm.

SI References

1. D. M. Baron *et al.*, Quantitative proteomics identifies proteins that resist translational repression and become dysregulated in ALS-FUS. *Hum Mol Genet* **28**, 2143-2160 (2019).
2. S. Boopathy *et al.*, Structural basis for mutation-induced destabilization of profilin 1 in ALS. *Proceedings of the National Academy of Sciences* **112**, 7984-7989 (2015).
3. Y. Perez-Riverol *et al.*, The PRIDE database and related tools and resources in 2019: improving support for quantification data. *Nucleic Acids Res* **47**, D442-D450 (2019).
4. A. Jegou, M. F. Carlier, G. Romet-Lemonne, Formin mDia1 senses and generates mechanical forces on actin filaments. *Nat Commun* **4**, 1883 (2013).
5. R. Gesztelyi *et al.*, The Hill equation and the origin of quantitative pharmacology. *Archive for History of Exact Sciences* **66**, 427-438 (2012).
6. K. J. R. B. J. M. B. L., Simultaneous analysis of multiple fluorescence decay curves: A global approach. *Chemical Physics Letters* **102**, 501-507 (1983).
7. O. Bilsel, J. A. Zitzewitz, K. E. Bowers, C. R. Matthews, Folding mechanism of the alpha-subunit of tryptophan synthase, an alpha/beta barrel protein: global analysis highlights the interconversion of multiple native, intermediate, and unfolded forms through parallel channels. *Biochemistry* **38**, 1018-1029 (1999).
8. L. Cao *et al.*, Modulation of formin processivity by profilin and mechanical tension. *Elife* **7** (2018).
9. A. Jegou *et al.*, Individual actin filaments in a microfluidic flow reveal the mechanism of ATP hydrolysis and give insight into the properties of profilin. *PLoS Biol* **9**, e1001161 (2011).
10. A. E. Cowan, Moraru, II, J. C. Schaff, B. M. Slepchenko, L. M. Loew, Spatial modeling of cell signaling networks. *Methods Cell Biol* **110**, 195-221 (2012).
11. A. S. Paul, T. D. Pollard, The role of the FH1 domain and profilin in formin-mediated actin-filament elongation and nucleation. *Curr Biol* **18**, 9-19 (2008).
12. J. Schaff, C. C. Fink, B. Slepchenko, J. H. Carson, L. M. Loew, A general computational framework for modeling cellular structure and function. *Biophys J* **73**, 1135-1146 (1997).
13. J. C. Phillips *et al.*, Scalable molecular dynamics with NAMD. *J Comput Chem* **26**, 1781-1802 (2005).
14. A. D. MacKerell *et al.*, All-atom empirical potential for molecular modeling and dynamics studies of proteins. *J Phys Chem B* **102**, 3586-3616 (1998).
15. W. Humphrey, A. Dalke, K. Schulten, VMD: visual molecular dynamics. *J Mol Graph* **14**, 33-38, 27-38 (1996).
16. J. P. Ryckaert, Ciccotti, G., & Berendsen, H. J. C. , Numerical integration of the cartesian equations of motion of a system with constraints: molecular dynamics of n-alkanes. *Journal of Computational Physics* **23**, 327-341 (1977).
17. B. J. Grant, A. P. Rodrigues, K. M. ElSawy, J. A. McCammon, L. S. Caves, Bio3d: an R package for the comparative analysis of protein structures. *Bioinformatics* **22**, 2695-2696 (2006).
18. A. Clauset, M. E. Newman, C. Moore, Finding community structure in very large networks. *Phys Rev E Stat Nonlin Soft Matter Phys* **70**, 066111 (2004).
19. A. B. Varshney, F.P.; Wright, W.V., Linearly Scalable Computation of Smooth Molecular Surfases. *IEEE Computer Graphics and Applications* (1994).
20. D. Frishman, P. Argos, Knowledge-based protein secondary structure assignment. *Proteins* **23**, 566-579 (1995).

21. M. Girvan, M. E. Newman, Community structure in social and biological networks. *Proc Natl Acad Sci U S A* **99**, 7821-7826 (2002).
22. L. Arike *et al.*, Comparison and applications of label-free absolute proteome quantification methods on Escherichia coli. *J Proteomics* **75**, 5437-5448 (2012).
23. B. Schwanhausser *et al.*, Global quantification of mammalian gene expression control. *Nature* **473**, 337-342 (2011).